



Label-free redox imaging of patient-derived organoids using selective plane illumination microscopy

PETER F. FAVREAU,¹ JIAYE HE,^{1,2,3} DANIEL A. GIL,^{1,4} DUSTIN A. DEMING,^{5,6,7,8} JAN HUISKEN,^{1,3}  AND MELISSA C. SKALA^{1,4,*}

¹Morgridge Institute for Research, Madison, WI 53715, USA

²Max Planck Institute for Molecular Cell Biology and Genetics, 01307 Dresden, Saxony, Germany

³Department of Integrative Biology, University of Wisconsin–Madison, Madison, WI 53715, USA

⁴Department of Biomedical Engineering, University of Wisconsin–Madison, Madison, WI 53715, USA

⁵University of Wisconsin Carbone Cancer Center, Madison, WI 53715, USA

⁶Division of Hematology and Oncology, Department of Medicine, University of Wisconsin–Madison, Madison, WI 53715, USA

⁷McArdle Laboratory for Cancer Research, Department of Oncology, University of Wisconsin–Madison, Madison, WI 53715, USA

⁸William S Middleton Memorial Veterans Hospital, Madison, WI 53715, USA

*mcskala@wisc.edu

Abstract: High-throughput drug screening of patient-derived organoids offers an attractive platform to determine cancer treatment efficacy. Here, selective plane illumination microscopy (SPIM) was used to determine treatment response in organoids with endogenous fluorescence from the metabolic coenzymes NAD(P)H and FAD. Rapid 3-D autofluorescence imaging of colorectal cancer organoids was achieved. A quantitative image analysis approach was developed to segment each organoid and quantify changes in endogenous fluorescence caused by treatment. Quantitative analysis of SPIM volumes confirmed the sensitivity of patient-derived organoids to standard therapies. This proof-of-principle study demonstrates that SPIM is a powerful tool for high-throughput screening of organoid treatment response.

© 2020 Optical Society of America under the terms of the [OSA Open Access Publishing Agreement](#)

1. Introduction

Patient-derived organoids are 3-D cultures, generated from fresh tumor samples, that capture phenotypic and genetic features of the original tumor while better recapitulating patient drug sensitivity compared to 2-D cultures [1,2]. Therefore, patient-derived organoids are an emerging platform for personalized high-throughput drug screens [3–5]. A single patient biopsy can generate tens to hundreds of organoids, permitting parallelized drug testing of standard therapies, drug combinations, and emerging treatments. However, existing high content, or information-rich approaches for organoid drug screens (e.g., immunofluorescence, RNAseq) are either low throughput, destructive, or both. Functional imaging of organoids could provide insight into early molecular changes with drug treatment, but relies on exogenous labels (e.g., antibodies, dyes, transfection with a fluorescent protein) that are difficult to implement on primary patient-derived cells. Additionally, dyes and antibody labels rely on 3-D diffusion for a uniform signal from all cells. Prolonged exposure to some dyes can also result in cellular toxicity, prohibiting long-term assessment. Conversely, high throughput approaches including plate reader assays and brightfield or epifluorescence microscopy are constrained by limited metrics to differentiate treatment response including viability and changes in organoid diameter, respectively [6,7]. Techniques like brightfield microscopy, epifluorescence microscopy, and plate readers lack optical sectioning and spatial specificity to assess the 3D morphology and function of organoids. These limitations

point to a need for label-free volumetric imaging of molecular features in organoids to more accurately assess changes in morphology and function with treatment response.

Cancer therapies often alter cellular metabolism either through direct targeting of metabolic pathways or as an early functional change before cell death. Fluorescence from metabolic co-enzymes NAD(P)H and FAD have been used to quantify dynamic changes in tumor cell metabolism [8–12] as an early marker of drug efficacy *in vivo* and in organoids [13–15]. The redox ratio, defined as the fluorescence intensity of NAD(P)H divided by the fluorescence intensity of FAD, is a well-studied metric of electron transfer rate and metabolic activity that does not require exogenous stains or dyes [16–20]. Notably, redox imaging is not amenable to resolving mechanisms of drug action but it can be combined with complementary measures such as proteomics, genomic sequencing, or metabolomics to resolve these mechanisms [21–23]. The fluorescence from NAD(P)H is indistinguishable from that of NADH, and will be referred to collectively as NAD(P)H. Many previous studies were performed using multiphoton microscopy to enable near-infrared excitation of these endogenous molecules, with the caveat of relatively low-throughput imaging due to the speed limit of raster scanning a 3-D volume [16,24–26].

Selective plane illumination microscopy (SPIM) operates by illuminating a single plane within the sample using a thin sheet of excitation light while fluorescence emission from this plane is collected by an orthogonally arranged objective. Like multiphoton microscopy, SPIM only excites fluorescence in the plane of interest, which provides optical sectioning and reduces out-of-plane phototoxicity [27,28]. Most notably, SPIM can image volumes more rapidly than multiphoton microscopy, and previous studies have imaged large numbers of organoids labeled with exogenous fluorescent markers [29–31]. To date, no studies have investigated label-free SPIM. SPIM also allows for simultaneous imaging of hundreds of organoids, which dramatically increases throughput when combined with fast imaging speeds.

Here, we present a study combining label-free contrast from NAD(P)H and FAD with SPIM's rapid volumetric recording capabilities to image entire patient-derived organoids and quantitatively assess response to standard cancer therapies. Organoids were imaged at a rate of ~ 0.2 s/organoid that ranged in diameter between 100–300 μm . NAD(P)H and FAD volumes were imaged with an average time of ~ 5 seconds per channel. We also demonstrate a novel shell-based segmentation algorithm to quantify organoid autofluorescence and the optical redox ratio from the surface to the core of each organoid. The ability to assess the metabolic state and 3-D morphological features of patient-derived organoids in a high-throughput framework offers exciting possibilities for improving drug screening and precision medicine.

2. Methods

2.1. Patient-derived organoid preparation and sample mounting

Cancer organoids were grown from a patient-derived metastatic colon cancer using a previously described protocol [32]. We adapted a standard FEP tube embedding protocol for organoid culture with Matrigel to culture several organoids for later evaluation with SPIM [33]. Organoids were singularized with 0.25% Trypsin, mixed with Matrigel at a 1:1 ratio, and allowed to grow for 12 days within modified FEP tubes and given modified DMEM/F12 media supplemented with Wnt-conditioned media from murine L-cells [Fig. 1(a)]. Modified FEP tubes were created from standard FEP tubes (1.6 mm/2.6 mm inner diameter/outer diameter, respectively, ProLiquid) cut to lengths of 3.5 cm. These smaller tubes were cut in half lengthwise to allow Matrigel droplets to be placed inside the FEP tube and fully exposed to feeding media and treatments. Each FEP tube was placed in a 1.5 mL Eppendorf tube to fully submerge each Matrigel droplet within the feeding media [Fig. 1(b)]. This method enables multiple Matrigel droplets, each with tens of organoids, to be placed in each tube [Fig. 1(c)].

After the initial growth period of 12 days, organoids were treated with media infused with standard therapies for colorectal cancer including either 10- μM 5-fluorouracil (5-FU, thymidylate

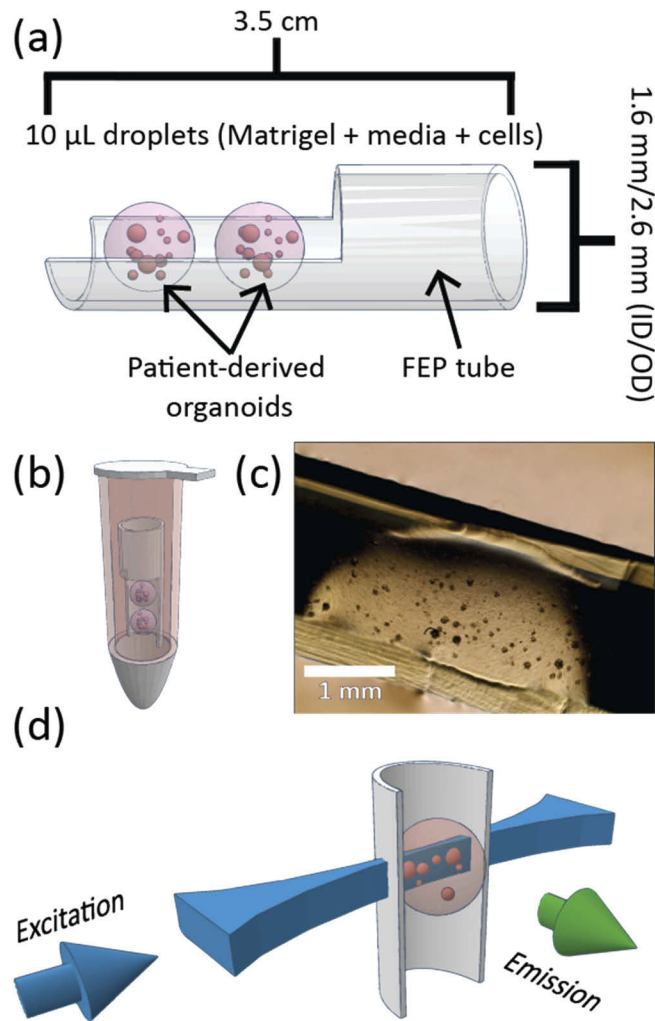


Fig. 1. Patient-derived organoid culture in modified FEP tubes for selective plane illumination microscopy. (a) Modified FEP tube with cut-out for easy organoid culture in Matrigel droplets. (b) Organoids were cultured in a 1.5 mL Eppendorf tube submerged in feeding media. (c) Image of organoids growing in FEP tube. (d) Diagram of excitation (blue arrow) and emission (green arrow) illustrating selective plane illumination of Matrigel droplets.

synthase inhibitor), 40- μ M Oxaliplatin (DNA synthesis inhibitor), or a combination of both treatments. Organoids were grown in treated media for 48 hours before imaging.

2.2. Immunofluorescence

Organoids were grown in a 24-well glass bottom dish for 12 days, then treated with either 10- μ M 5-FU, 40- μ M oxaliplatin, or a combination of both treatments. After 48 hours, organoids were rinsed in phosphate buffered saline (PBS) and fixed for 30 minutes in 4% paraformaldehyde (VWR). Fixed organoids were rinsed twice and stored in PBS at 4°C until staining. Organoids were blocked for one hour in PBS with 10% goat serum and 0.3% Triton-X 100 (Sigma) at room temperature followed by co-incubation with Ki-67 antibody conjugated to AlexaFluor 488 (1:50, Cell Signaling #11882S) and CC3 antibody conjugated to AlexaFluor 555 (1:50,

Cell Signaling #9604S). Organoids were washed in PBS and mounted to a slide using ProLong Diamond Antifade Mountant with DAPI (Molecular Probes). DAPI was imaged on a custom-built multiphoton microscope with a 40x objective (Nikon CFI APO Lambda S, 1.15 NA) using 750 nm for excitation and 440/80 nm bandpass filter for emission. AlexaFluor 488 was imaged using 965 nm for excitation and 550/100 nm filter for emission. AlexaFluor 555 was imaged using 1050 nm excitation and a 585/65 nm filter. At least three organoids were imaged per treatment group to canvas treatment response.

We also calculated the percentage of pixels with cleaved Caspase-3 labeling across the diameter of immunolabeled organoids. Cleaved Caspase-3-labeled pixels were measured along the diameter of each organoid, and the diameter of each immunolabeled organoid was measured from the center slice of the organoid. For nine organoids, the average percentage of pixels with cleaved Caspase-3 across the organoid diameter was 27.5%, with labeling predominantly in the periphery and the innermost portions of each organoid. For the shell-based approach, we have chosen a more conservative percentage (20%) to limit rejection of viable cells.

2.3. Selective Plane Illumination Microscopy

Imaging was performed using a custom-built multi-directional SPIM based on a previous design [34] [Fig. 1(d)]. A total of 238 organoids were imaged, with a range of 39-60 organoids for each treatment condition. Illumination of NAD(P)H and FAD was performed using a fiber-coupled laser engine (Toptica MLE, Toptica) at 405 nm and 488 nm, respectively. A 440/80 nm emission filter and 550/100 nm emission filter was used to collect NAD(P)H and FAD emission, respectively. Two 10X water dipping objectives (UMPLFLN10XW, Olympus) were used to illuminate the sample in two opposing directions to increase imaging coverage. One 20X water dipping objective (UMPLFLN20XW) is used for fluorescence detection. An sCMOS camera (Andor Zyla 4.2 PLUS, Andor) was used to acquire images at 2048×2048 -pixel resolution at 100 frames per second. The light sheet was formed statically using standard Gaussian optics and a cylindrical lens with a waist thickness of roughly 6 μm . Illumination laser power was measured to be ~ 5.5 mW at the back focal plane of the illumination objective. A heated water bath was used during imaging for temperature control. Volumetric imaging of NAD(P)H and FAD was performed sequentially, with a ~ 5 s average acquisition time in each channel. The diameter of organoids ranged between 100-300 μm with a voxel size of 0.325 μm in x and y, and 2 μm in z.

2.4. 2-D intensity thresholding organoid volumes

A custom-built intensity thresholding algorithm was developed in MATLAB and used to analyze the FAD and NAD(P)H intensities at each optical slice. A three-dimensional median filter was performed with a kernel size of 3 $\mu\text{m} \times 1 \mu\text{m} \times 9 \mu\text{m}$, then the mean background value was subtracted from the volume. All pixels less than the mean background value were set equal to 0. Then the image was thresholded for all pixels greater than the mean background value plus 1. All 3-D regions less than 10^3 pixels were removed using standard mathematical morphology approaches (*bwareaopen*, MATLAB). All holes within the segmented organoid were filled (*imfill*, MATLAB), then a 3-D Gaussian filter was applied to smooth boundaries. The mask was applied to the NAD(P)H volume, the FAD volume, and the redox volume and the mean was calculated on a per slice basis.

2.5. Shell-based quantification algorithm

We developed a shell-based quantification algorithm to quantify treatment response in organoids as a function of radial distance from the organoid outer surface. This algorithm first performs 3-D segmentation of organoids within each SPIM volume using fuzzy C-means clustering and shape-based analysis (sphericity and size) to select for organoids and exclude cell-debris. Each SPIM volume contains between 3 and 15 organoids. The shell-based segmentation seeks to

create hollow 3-D surfaces (shells) with decreasing volume to quantify the pixel values in each shell. The shell analysis algorithm begins with a non-spherical, 3-D logical mask of the original organoid. The shells are created through an iterative process where this mask is eroded by a set number of pixels and then subtracted from the mask of the previous iteration. This yields shells that conform to the non-spherical morphology of the organoid. We used a spherical structure element ('strel', MATLAB) for the erosion operation because it uniformly removed the desired number of pixels from the original non-spherical mask. Other 3-D structure elements (cube, cuboid) caused artifacts in which the shells had discontinuous regions. The shell-based algorithm permits quantification of NAD(P)H, FAD, and optical redox ratio as a function of radial distance from the organoid surface while rejecting the influence of the necrotic core and outermost cells of organoids. Additionally, segmentation of each organoid permits morphological analysis of the volume.

2.6. Sphericity calculation

Sphericity of organoids was calculated with the following equation:

$$\Psi = \frac{\pi^{\frac{1}{3}}(6V_{org})^{\frac{2}{3}}}{A_{org}}$$

where V_{org} and A_{org} are the measured volume and surface area of the organoid, respectively. A value that approaches 1 is more spherical, while a value that approaches 0 is less spherical.

2.7. Redox ratio and diameter measurements with multiphoton and brightfield imaging

SPIM measurements were confirmed using multiphoton imaging and brightfield microscopy. A custom-built multiphoton microscope equipped with a 40X water immersion objective (Nikon CFI APO Lambda S, 1.15 NA) was used to acquire NAD(P)H and FAD fluorescence. NAD(P)H fluorescence was captured using a 440/80 nm filter cube, and FAD fluorescence was captured using a 550/100 nm filter cube. At least 11 total fields-of-view were acquired over 3 separate imaging days for each treatment group. Treatments were given to patient-derived colorectal cancer organoids as described earlier, with organoids cultured in 35-mm round coverslips for multiphoton imaging. After 48 hours, organoids were imaged using both multiphoton and brightfield microscopy for fluorescence and diameter measurements, respectively.

3. Results

3.1. SPIM redox imaging of patient-derived colorectal cancer organoids

Patient-derived organoids were grown from single cell suspensions and cultured in modified FEP tubes. SPIM redox imaging was performed with organoids treated for 48 hours with standard colorectal cancer treatments [35], including 10 μ M 5-fluorouracil (5-FU), 40 μ M Oxaliplatin, and a combination of 5-FU and oxaliplatin. A representative maximum intensity projection of one organoid volume treated with 5-FU is shown in Fig. 2(a). A supplemental movie ([Visualization 1](#)) showing the complete organoid volume in Fig. 2 has been included. The large organoid in Fig. 2(a) displays a prominent core with a bright FAD signal in the center of the organoid (red arrow). Critically, this volume was acquired in less than 10 seconds without contrast from exogenous labels. While not a universal feature of all organoids, each organoid shown in Fig. 2 features cells around the exterior with high FAD fluorescence [Figs. 2(b)–2(d), orange boxes]. The 2-D images of the smaller organoids taken at increasing z-depth display nuclear outlines of cells [Figs. 2(b)–2(d)].

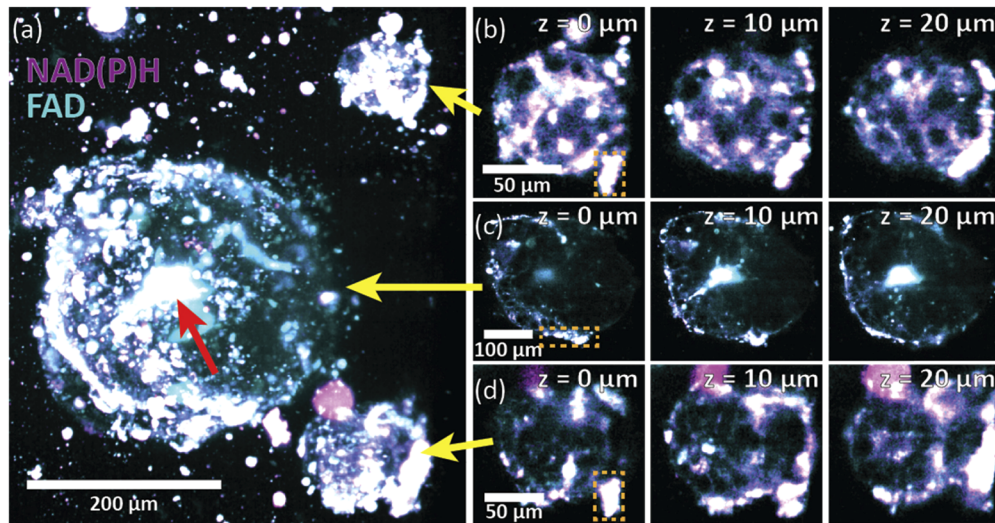


Fig. 2. Representative images of colorectal cancer organoids acquired with SPIM. The contrast from NAD(P)H and FAD is shown in magenta and blue, respectively. (a) Maximum intensity projection of three organoids. (b-d) Selected optical slices of each organoid cropped from the maximum intensity projection in (a). Yellow arrows show the location of each organoid in the maximum intensity projection in (a). Orange boxes cells around the exterior of organoids with high FAD fluorescence.

3.2. Per-slice analysis of organoid fluorescence

A custom-built intensity thresholding algorithm was used to analyze NAD(P)H and FAD intensities at each optical slice (see Methods, Section 2.4). A representative organoid, treated with 10 μ M 5-FU, was analyzed with this 2-D approach (Fig. 3). We found three regions, outlined in the plot by red boxes, that illustrate three distinct intensity profiles within the organoid. High fluorescence intensities from both NAD(P)H and FAD correspond to brighter regions in the center of the organoid, or regions lining the periphery of the organoid. These brighter regions also correspond to lower redox ratios, which have previously been reflective of a response to treatment [13,32].

3.3. Immunofluorescence of organoids

To better understand the spatial distribution of responsive and non-responsive cells in an organoids, the presence of apoptotic and proliferative regions was investigated using immunofluorescence of Ki-67, cleaved caspase 3 (CC3), and DAPI (Fig. 4). Figure 4 shows representative images acquired through the center of each organoid using multiphoton microscopy and immunofluorescence staining of the same patient-derived colorectal cancer organoid line imaged with SPIM. Z-stacks were acquired for each field-of-view to determine uniform labeling throughout each organoid. The untreated [Fig. 4(a)] and 5-FU-treated [Fig. 4(b)] organoids showed minimal CC3 expression (apoptosis) and high expression of Ki-67 (proliferation) throughout.

Conversely, oxaliplatin [Fig. 4(c)] and combination-treated [Fig. 4(d)] organoids displayed significant CC3 expression and less Ki-67 expression, indicating increased apoptosis and less proliferation compared to untreated and 5-FU-treated organoids. Perhaps most interesting is the organization of cellular layers within the combination-treated organoids. Apoptotic cells surround the periphery and comprise the inner core of the organoid. A transition zone of proliferating cells

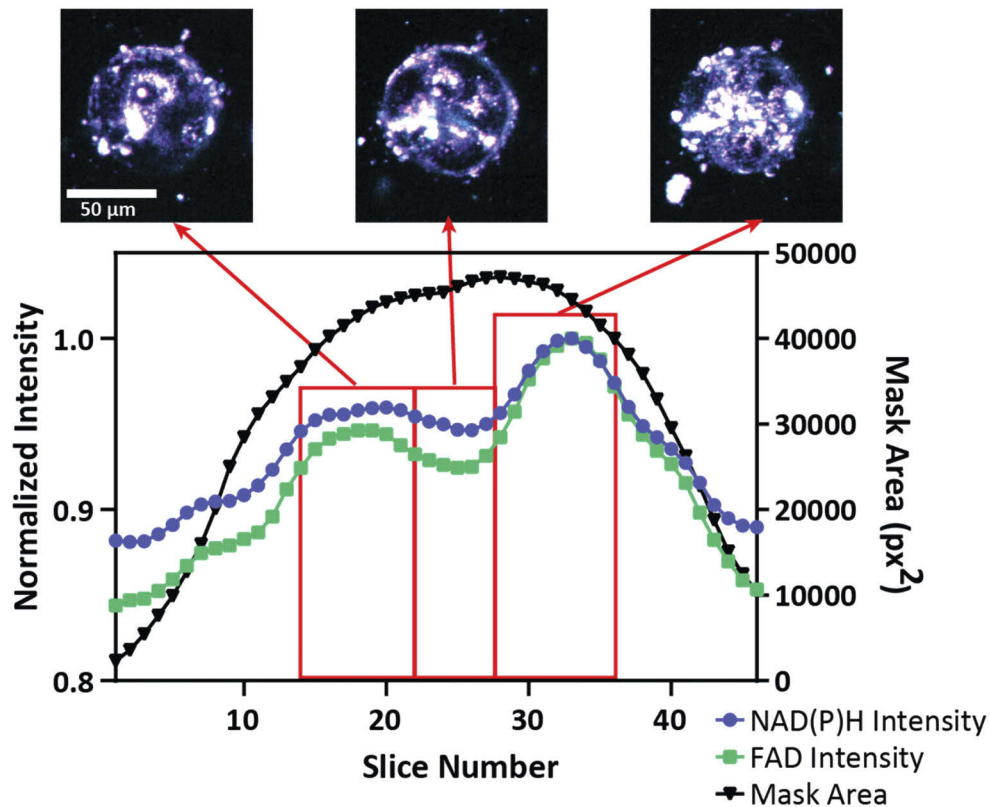


Fig. 3. 2-D analysis of organoid volumes using intensity thresholding. The intensity of NAD(P)H (blue) and FAD (green) were normalized to the maximum intensity across all optical slices. The occupied area of each mask as a function of slice number is shown on the right Y-axis. The maximum intensity projection for a range of optical slices is shown above the plot, with corresponding intensities and mask areas demarcated by red boxes.

is located between these two apoptotic layers. Given these distinct cell locations, we developed methods to quantify treatment response with radial distance from the organoid outer surface.

3.4. Shell-based 3-D segmentation of organoid volumes

A shell-based 3-D analysis was developed to better isolate treatment response from proliferative cells while ignoring fluorescence from apoptotic cells. Figure 5 uses a representative organoid treated with 5-FU to illustrate the quantitative output by the 3-D segmentation algorithm. The purpose of the 3-D analysis is to create 3-D shells with decreasing volume and quantify the fluorescence intensities in each shell. A non-spherical, 3-D logical mask is initially created from the shape of the organoid as an outer mold. A spherical structure element is then subtracted iteratively from the logical mask, each time yielding a hollow 3-D shell that permits quantification of NAD(P)H, FAD, and the optical redox ratio. Figure 5(a) shows a maximum intensity projection of a representative organoid treated with 10 μM 5-FU. Contrast from NAD(P)H and FAD is displayed in magenta and blue, respectively. A high intensity inner core region is shown where FAD fluorescence predominates. Figure 5(b) illustrates a model of an organoid, with shells marked with different colors to show how shells are demarcated. A red arrow is used to indicate the core region in Fig. 5(a) represented in the model organoid of Fig. 5(b). For clarity, shells have been converted to the distance, in microns, from the outermost shell. Figures 5(c)–5(d) show the

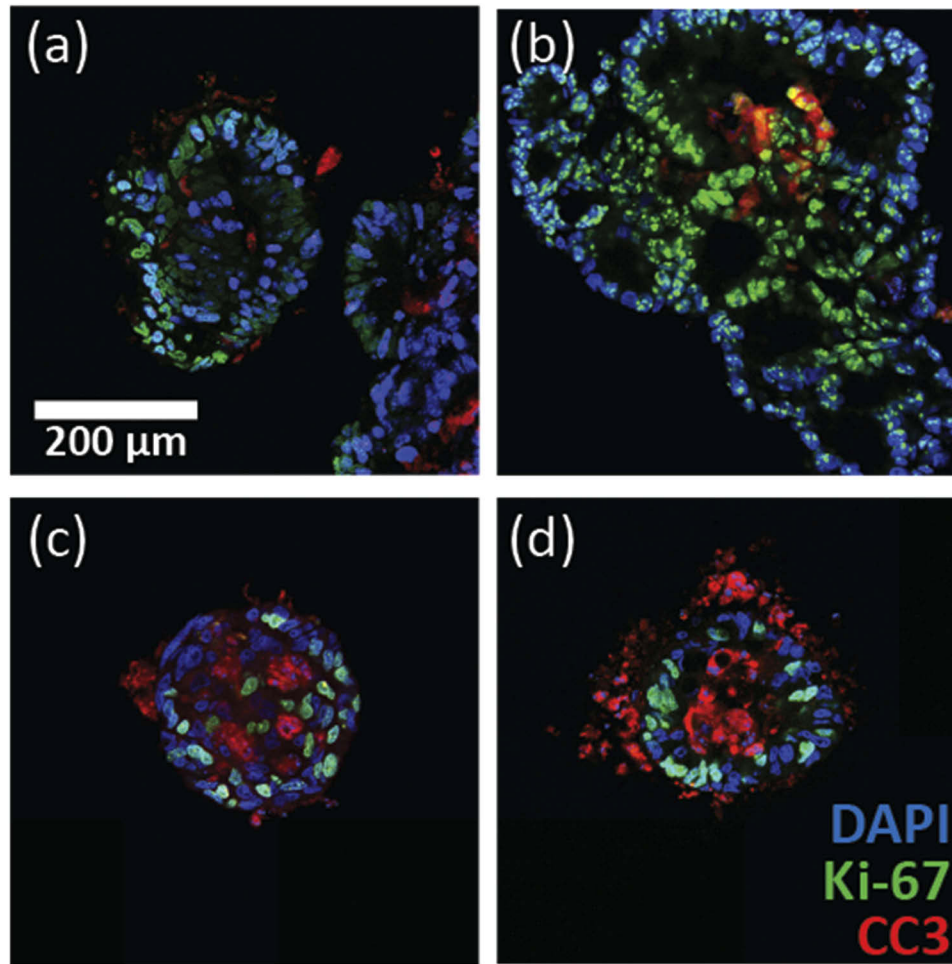


Fig. 4. Immunofluorescence of patient-derived colorectal cancer organoids with either (a) no treatment, (b) 5-FU, (c) oxaliplatin, or (d) combination treatments. Images were acquired through the center of each organoid volume. Blue: DAPI, green: Ki-67, red: cleaved-caspase 3.

NAD(P)H intensity, FAD intensity, and optical redox ratio as a function of outer edge distance for the organoid shown in Fig. 5(a). Three regions are highlighted as boxes in Figs. 5(c)–5(d), denoting the outermost shell (black), proliferative zone (gray), and the inner core region (red). 3-D illustrations of each shell region are shown above their respective boxes. The innermost region, corresponding primarily to the core region [36], includes cells with the highest standard deviation in NAD(P)H intensity, FAD intensity, and optical redox ratio. Critically, as the shell segmentation approaches the innermost core region, the FAD intensity increases relative to the NAD(P)H intensity, driving the redox ratio lower.

3.5. Redox ratio trends across treatments

To investigate general trends in the redox ratio following treatment we compared the redox ratio results for the first 75 μm (i.e. 100 shells) across all organoids in each treatment category. The first 100 shells were chosen to compare treatments across at least 10 organoids. Figure 6(a) displays a heatmap of the difference between the median redox ratio across all organoids for

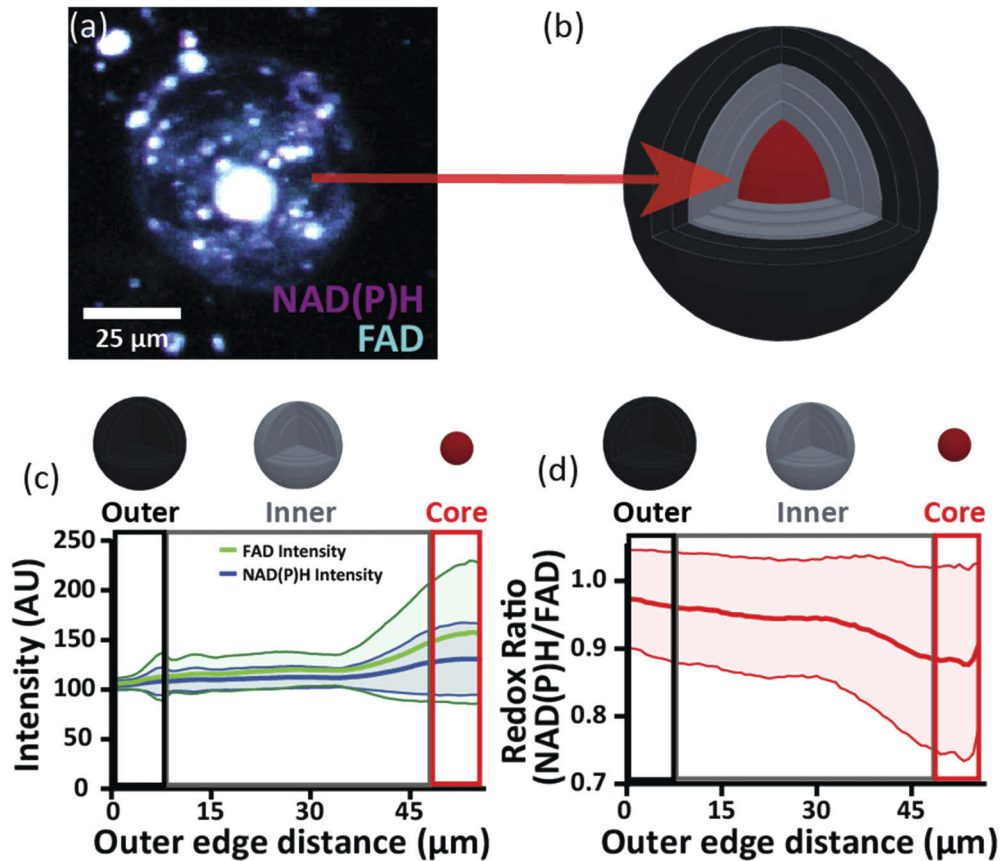


Fig. 5. Shell-based analysis overview. (a) Representative maximum intensity image of a colorectal organoid with a prominent core region (arrow). (b) 3-D spherical model for shell analysis. (c) NAD(P)H (blue) and FAD (green) intensity plots as a function of shell number. Note that an outer edge distance of 0 μm corresponds to the outermost shell, with increasing outer edge distance corresponding to decreasing distance from the innermost shell. Each colored box (black, gray, or red) corresponds to either the outer, inner, or core regions of the organoid, respectively. A 3-D rendering of each region is shown above their respective colored box. (d) The optical redox ratio as a function of shell number. Shaded regions in each plot are standard deviations of intensity or redox ratio at each outer edge distance.

that distance from the outermost shell versus the median redox ratio across all untreated control organoids for that distance from the outermost shell. A cutoff point of 75 μm (or 100 shells) was used to ensure a high number of organoids were included in the statistical calculation of the redox ratio at each outer edge distance.

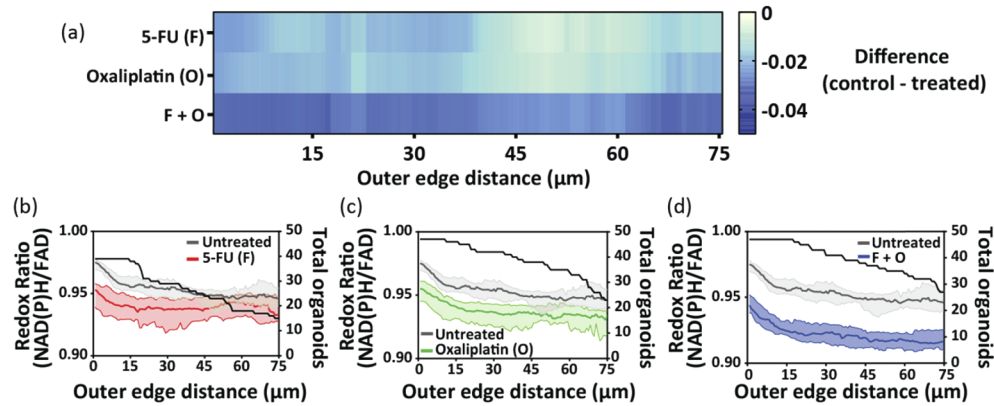


Fig. 6. Response across all treatments as a function of shell number. (a) Heatmap of the difference between the median redox ratio across all organoids for each treatment versus the median redox ratio of the control organoids as a function of shell number. Blue represents a decrease in redox ratio relative to control. (b-d) Individual comparisons between treatment and control of the median redox ratio across all organoids treated with 5-FU, Oxaliplatin, and combination, respectively. Shaded regions represent 95% CI at each shell number.

Notably, all treatments were at least marginally effective in lowering the redox ratio, with significant decreases shown in darker shades of blue. 5-FU displayed the least reduction in redox ratio for the first 75 μm , corresponding to a marginal treatment response. Conversely, Oxaliplatin and combination-treated organoids displayed a decreased redox ratio compared to control across the entire distance from the outermost layer. The combination therapy displayed the most reduction in the redox ratio throughout all shells, consistent with the expected treatment response. Figures 6(b)–6(d) plots the response for each treatment as a function of median redox ratio compared to control. The solid black line represents the number of organoids used in calculating the median redox ratio at that distance from the outer edge.

Consistent with Fig. 6(a), 5-FU displays a similar redox ratio to untreated as outer edge distance increases [Fig. 6(b)], Oxaliplatin shows a higher response than 5-FU [Fig. 6(c)], and organoids treated with combination therapy display the most reduction in redox ratio compared to control.

3.6. Cumulative fluorescence and morphologic treatment response from organoids

Next, we plotted the redox ratio across all organoids while attempting to exclude regions that can contain significant apoptotic cell populations (i.e. the first 10% and last 10% of shells). The shell-based approach also permits 3-D morphologic assessment of organoids, which was used to compare volumes and sphericity across organoids after treatment. Violin plots were used to show variance within treatment groups with the black line indicating the median value. Sphericity was calculated using the surface area and volume measurements for each organoid (see Methods). The redox ratio results [Fig. 7(a)] indicate significant reductions for each treatment compared to control, especially for the Oxaliplatin and combination therapies. Figure 7(b) shows the average volume across organoids separated by treatment. There was high variation between treatment groups, with the highest variation in volume from combination-treated organoids. No significant difference in volume was measured. Conversely, significant differences in sphericity were identified in the Oxaliplatin and combination therapies [Fig. 7(c)].

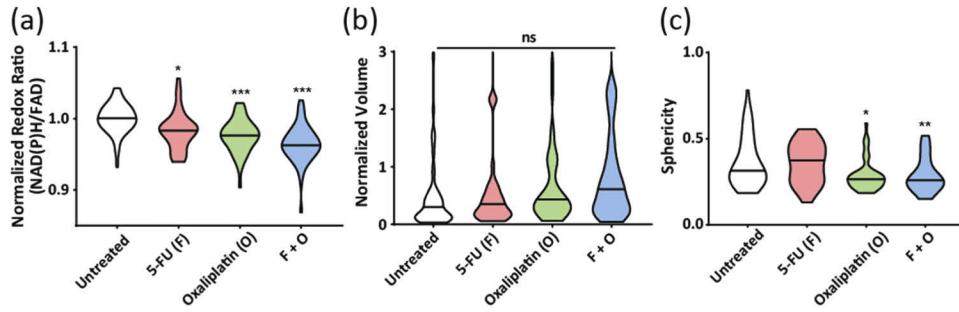


Fig. 7. Quantitative image analysis of colorectal cancer organoid treatment response measured using SPIM volumes. (a) Violin plots showing the optical redox ratio of organoid SPIM volumes analyzed with a shell-based algorithm approach and normalized to the maximum redox ratio within a treatment group. The normalized redox ratio is calculated by normalizing the redox ratio of each organoid to the average redox ratio for control organoids. The first 10% and last 10% of shells were ignored to mitigate potential influence from the outermost and innermost shell regions that typically contain apoptotic cells. (b) Organoid volumes normalized to the average volume within a treatment group. (c) Sphericity of organoids calculated using the measured volume and surface area of each organoid within a treatment group. * $p < 0.05$, ** $p < 0.005$, *** $p < 0.001$; black lines are the median value.

We also investigated whether a correlation existed between the organoid diameter and the redox ratio but found no correlation both within treatment groups and across all organoids (Fig. 8).

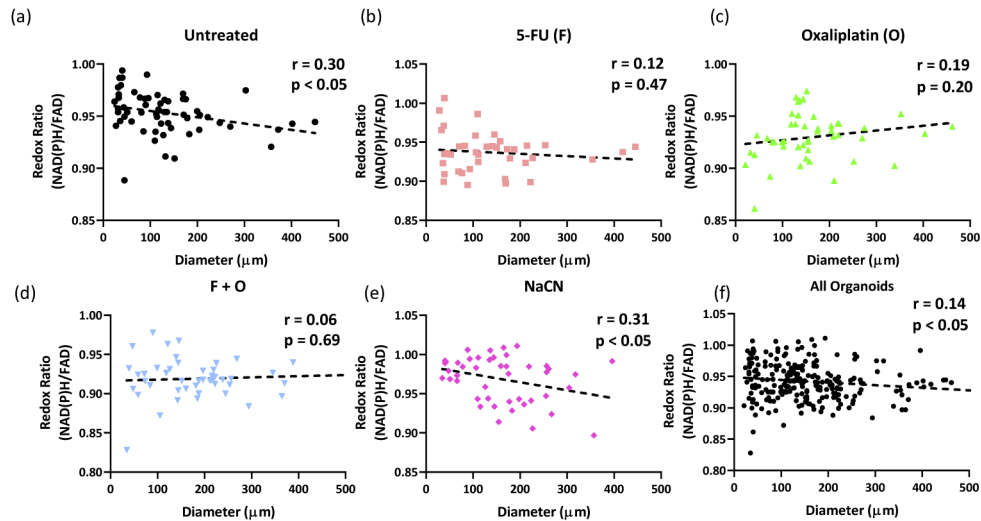


Fig. 8. Linear regression of organoid diameter and redox ratio. (a-e) Plots with all organoids from each treatment group. (f) Regression analysis of all organoids together.

3.7. Validation of SPIM redox imaging with multiphoton and brightfield microscopy

The fluorescence and diameter measurements were validated by imaging organoids treated with the same conditions as the SPIM experiments but imaged using well-studied multiphoton and brightfield microscopes [25,37]. Figure 9(a) shows redox ratio results from multiphoton microscopy averaged across all organoids per treatment and normalized to untreated organoids. A significant decrease in redox ratio was shown for Oxaliplatin and combination (5-FU and

Oxaliplatin), consistent with SPIM measurements. Using brightfield microscopy, no change in diameter was measured between treatment groups after 48 hours [Fig. 9(b)], consistent with volumetric measurements acquired using SPIM.

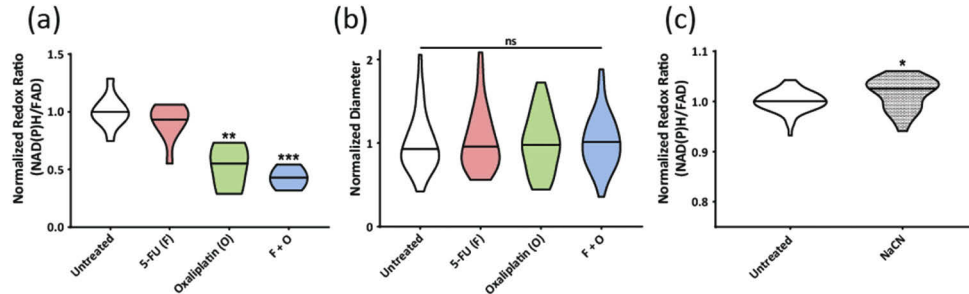


Fig. 9. Validation measurements of SPIM redox imaging. (a) Multiphoton imaging of patient-derived colorectal cancer organoids. (b) 2-D diameter measurements of CRC organoids acquired with brightfield microscopy. (c) SPIM imaging of CRC organoids treated with 10-mM NaCN.

Previous optical metabolic imaging studies used cyanide as a positive control to assess sensitivity to metabolic perturbations. Therefore, this treatment was repeated on the SPIM system as a secondary control. Untreated organoids were given media supplemented with 10-mM NaCN to determine whether organoids will respond to NaCN as described previously [9,38]. Predictably, organoids showed a statistically significant increase in redox ratio relative to control after 45 minutes of NaCN treatment [Fig. 9(c)].

4. Discussion

To our knowledge, this is the first time SPIM has been used to image live organoid cultures without labels. Previous work with organoid cultures has involved the addition of exogenous labels or the use of label-free multiphoton microscopy [4,15,39]. Label-free multiphoton microscopy has shown promise in discriminating treatment response patient-derived organoid cultures, including colorectal cancer organoids [14,36]. In this study, drug response was discriminated in patient-derived colorectal cancer organoids using label-free SPIM. Drug response was assessed by measuring the redox ratio using fluorescence from the metabolic co-enzymes NAD(P)H and FAD on a per-organoid level (Fig. 2).

The described label-free SPIM approach offered a substantial improvement over existing high content, or information-rich technologies. High content methods for measuring treatment response in organoids, such as RNAseq or immunofluorescence, are inherently destructive and lack the ability to measure the organoids in real time [40,41]. Conversely, label-free SPIM permitted rapid imaging at a rate of ~ 0.2 s/organoids and offered a non-destructive platform to measure fluorescence. Fluorescence from NAD(P)H and FAD provided contrast based on the amount of electron donors and acceptors within cells or organoids, which allows the quantification of metabolic shifts due to treatment response. Morphologic features, including volume and surface area, were also measured and used to calculate the sphericity of each organoid. The change in redox ratio and sphericity versus control were in agreement [Figs. 7(a) and 7(c)], suggesting that a combined metric calculated from both variables may provide improved discrimination of treatment response. Additionally, the reduced sphericity of organoids could also be due to subpopulations of resistant cells. Further optimization of our imaging approach may discriminate individual cells across whole volumes, providing both organoid level and single cell level interrogation of drug resistance.

Label-free SPIM performed in this study also highlights improvements over other high-throughput assessment technologies. Standard non-imaging plate readers can assess treatment-induced changes in redox ratio in cell monolayers, but no studies have measured the redox ratio in unlabeled patient-derived organoids [39,42]. In addition, plate readers lack spatial information, which prevents the assessment of inter- and intra-organoid heterogeneity. Brightfield microscopy can be used to rapidly assess organoids, and response is widely determined through measurements of organoid diameter performed by hand, which can introduce bias and interobserver disagreement. Brightfield also captures a 2-D projection of the organoid, ignoring the 3-D nature of organoids. SPIM is a marked improvement over brightfield as it captures the entire 3-D volume of organoids, limiting measurement bias and interobserver disagreement. Epifluorescence is an alternative technology that can readily image NAD(P)H and FAD fluorescence, but again only in a 2-D projection that lacks the full 3-D information of the organoid. However, both plate readers and standard microscopy approaches use standard culture dishes and data can be collected without significant attention paid to data storage. SPIM volumes require substantial data storage, with each set of NAD(P)H and FAD volumes averaging 4-5 GB in size. Thus, drug screening platforms featuring SPIM must also include appropriate storage and data parsing support.

After investigating the distribution of proliferative and apoptotic cells in organoids post-treatment (Fig. 4), a custom-made 3-D shell segmentation algorithm was developed to better model and quantify each organoid. While traditional approaches the organoid as a single region or made up of optical, the shell-based approach offered an opportunity to limit the inclusion of the dense core region and outer debris seen in highly treatment-responsive organoids (Fig. 5). In general, this approach highlights changes in fluorescence and redox ratio relative to the outer edge of each organoid. This enabled parsing the overall trends of the redox ratio in separate treatment groups as distance from the outer edge increased toward the inner core region (Fig. 6). Importantly, for small distances from the outer edge, the redox ratio tended toward larger differences between control, while the opposite was true for distances further from the outer edge except for the combination treatment. While Fig. 6 shows only distances up to 75 μm from the outer edge to plot as many organoids as possible, the redox ratio was measured for the largest organoids (up to 225 μm) with similar trends. This approach opens the door for more resolved treatment response across organoid volumes, and better interrogation of treatment-resistant cell niches that may be present in a patient's tumor and result in disease recurrence.

Successful 3-D imaging of patient-derived organoids in the custom-built SPIM system also required adapting the standard organoid culturing preparation [7,36]. To appropriately culture, treat, and image the colorectal cancer organoids over multiple weeks, organoids were cultured within FEP tubes with part of the tube cut away to expose the organoids to feeding media [Figs. 1(a) and 1(b)]. Techniques based on oblique light sheets such as oblique plane microscopy would enable imaging organoids within standard culture dishes [34,43], which would allow for longitudinal measurements to assess time-dependent changes in redox ratio and organoid morphology due to treatment.

Our results agreed with established methods of determining treatment response (i.e. multiphoton redox ratio imaging and brightfield diameter measurements), with the multiphoton results showing larger relative differences between treatment groups. It's likely these differences stem from the improved signal-to-noise ratio and higher quantum efficiencies from photomultiplier tubes used in the multiphoton system [26,36]. An additional consideration is the depth penetration of the light sheet compared to the high out-of-focus rejection using a multiphoton approach. High scattering effects in larger organoids present a challenging obstacle for widefield detection schemes. We performed a preliminary calculation of the attenuation using values for the scattering and absorption coefficients of skin and water, respectively (data not shown). As expected, higher attenuation occurs at the emission wavelengths for NAD(P)H than for FAD. It is likely that this effect is small in organoids with shell-based analysis, as no relationship between the redox ratio

and organoid diameter was found (Fig. 8). However, a two-sided detection scheme would provide a hardware solution to mitigate wavelength-dependent attenuation effects.

As precision oncology continues to progress, better drug screening is required to enable more personalized cancer therapies. Organoid cultures have offered a powerful tool toward personalized treatments, but methods of discriminating treatment response are often sample-destructive or low-throughput. In this study, we determined treatment response in patient-derived organoids using label-free SPIM. These preliminary results show the potential for label-free fluorescence imaging of treatment response across entire volumes of patient-derived organoids, which could enable new 3-D high-throughput drug screens of clinical samples. This work also presents a novel 3-D shell-based approach to quantify morphological and functional readouts of treatment response. SPIM combined with this quantification approach enabled comparisons based on fluorescence, volume, and sphericity, opening the door for more holistic personalized drug screens without sacrificing information content or imaging speed. Altogether, label-free SPIM provides a promising high-throughput and high-content platform to improve organoid-based drug screens for personalized oncology.

Funding

National Science Foundation (CBET-1642287); Stand Up To Cancer (SU2C-AACR-IG-08-16, SU2C-AACR-PS-18); National Institutes of Health (R01 CA185747, R01 CA205101, R01 CA211082, R21 CA224280, R37 CA226526, U01 TR002383); University of Wisconsin Carbone Cancer Center (P30 CA014520).

Acknowledgments

We would like to acknowledge the artwork of Jacki Whisenant for assisting the models in Figs. 1(a), (b), and (d). The authors also thank Joseph Sharick for his support with the organoid immunofluorescence protocol.

The Skala laboratory is supported by grants from the NSF (CBET-1642287), Stand Up to Cancer (SU2C-AACR-IG-08-16, SU2C-AACR-PS-18) and the NIH (R01 CA185747, R01 CA205101, R01 CA211082, R21 CA224280, U01 TR002383). The Deming laboratory is supported by the NIH (R37 CA226526) and the University of Wisconsin Carbone Cancer Center (Support Grant P30 CA014520 and the UWCCC Pancreatic Cancer Taskforce). We would also like to acknowledge support by the Morgridge Institute for Research.

Disclosures

The authors declare that there are no conflicts of interest related to this article.

References

1. J. Drost and H. Clevers, "Organoids in cancer research," *Nat. Rev. Cancer* **18**(7), 407–418 (2018).
2. A. Fatehullah, S. H. Tan, and N. Barker, "Organoids as an in vitro model of human development and disease," *Nat. Cell Biol.* **18**(3), 246–254 (2016).
3. F. Weeber, S. N. Ooft, K. K. Dijkstra, and E. E. Voest, "Tumor Organoids as a Pre-clinical Cancer Model for Drug Discovery," *Cell Chem. Biol.* **24**(9), 1092–1100 (2017).
4. G. Vlachogiannis, S. Hedayat, A. Vatsiou, Y. Jamin, J. Fernández-Mateos, K. Khan, A. Lampis, K. Eason, I. Huntingford, R. Burke, M. Rata, D.-M. Koh, N. Tunariu, D. Collins, S. Hulkki-Wilson, C. Ragulan, I. Spiteri, S. Y. Moorcraft, I. Chau, S. Rao, D. Watkins, N. Fotiadis, M. Bali, M. Darvish-Damavandi, H. Lote, Z. Eltahir, E. C. Smyth, R. Begum, P. A. Clarke, J. C. Hahne, M. Dowsett, J. de Bono, P. Workman, A. Sadanandam, M. Fassan, O. J. Sansom, S. Eccles, N. Starling, C. Braconi, A. Sottoriva, S. P. Robinson, D. Cunningham, and N. Valeri, "Patient-derived organoids model treatment response of metastatic gastrointestinal cancers," *Science* **359**(6378), 920–926 (2018).
5. D. Dutta, I. Heo, and H. Clevers, "Disease Modeling in Stem Cell-Derived 3D Organoid Systems," *Trends Mol. Med.* **23**(5), 393–410 (2017).

6. T. Grabinger, L. Luks, F. Kostadinova, C. Zimmerlin, J. P. Medema, M. Leist, and T. Brunner, "Ex vivo culture of intestinal crypt organoids as a model system for assessing cell death induction in intestinal epithelial cells and enteropathy," *Cell Death Dis.* **5**(5), e1228 (2014).
7. N. Sachs, J. de Lig, O. Kopper, E. Gogola, G. Bounova, F. Weeber, A. V. Balgobind, K. Wind, A. Gracanin, H. Begthel, J. Korving, R. van Boxtel, A. A. Duarte, D. Lelieveld, A. van Hoeck, R. F. Ernst, F. Blokzijl, I. J. Nijman, M. Hoogstraat, M. van de Ven, D. A. Egan, V. Zinzalla, J. Moll, S. F. Boj, E. E. Voest, L. Wessels, P. J. van Diest, S. Rottenberg, R. G. J. Vries, E. Cuppen, and H. Clevers, "A Living Biobank of Breast Cancer Organoids Captures Disease Heterogeneity," *Cell* **172**(1-2), 373–386.e10 (2018).
8. T. M. Heaster, A. J. Walsh, and M. C. Skala, "Differentiating quiescent cancer cell populations in heterogeneous samples with fluorescence lifetime imaging," in (International Society for Optics and Photonics, 2016), Vol. 9719, p. 97190L.
9. A. J. Walsh, R. S. Cook, H. C. Manning, D. J. Hicks, A. Lafontant, C. L. Arteaga, and M. C. Skala, "Optical Metabolic Imaging Identifies Glycolytic Levels, Subtypes, and Early-Treatment Response in Breast Cancer," *Cancer Res.* **73**(20), 6164–6174 (2013).
10. M. C. Skala, K. M. Riching, A. Gendron-Fitzpatrick, J. Eickhoff, K. W. Eliceiri, J. G. White, and N. Ramanujam, "In vivo multiphoton microscopy of NADH and FAD redox states, fluorescence lifetimes, and cellular morphology in precancerous epithelia," *Proc. Natl. Acad. Sci. U. S. A.* **104**(49), 19494–19499 (2007).
11. K. Alhallak, L. G. Rebello, T. J. Muldoon, K. P. Quinn, and N. Rajaram, "Optical redox ratio identifies metastatic potential-dependent changes in breast cancer cell metabolism," *Biomed. Opt. Express* **7**(11), 4364–4374 (2016).
12. A. Varone, J. Xylas, K. P. Quinn, D. Pouli, G. Sridharan, M. E. McLaughlin-Drubin, C. Alonzo, K. Lee, K. Munger, and I. Georgakoudi, "Endogenous two-photon fluorescence imaging elucidates metabolic changes related to enhanced glycolysis and glutamine consumption in precancerous epithelial tissues," *Cancer Res.* **74**(11), 3067–3075 (2014).
13. A. J. Walsh, R. S. Cook, M. E. Sanders, L. Aurisicchio, G. Ciliberto, C. L. Arteaga, and M. C. Skala, "Quantitative Optical Imaging of Primary Tumor Organoid Metabolism Predicts Drug Response in Breast Cancer," *Cancer Res.* **74**(18), 5184–5194 (2014).
14. A. J. Walsh, J. A. Castellanos, N. S. Nagathihalli, N. B. Merchant, and M. C. Skala, "Optical Imaging of Drug-Induced Metabolism Changes in Murine and Human Pancreatic Cancer Organoids Reveals Heterogeneous Drug Response," *Pancreas* **45**(6), 863–869 (2016).
15. A. T. Shah, T. M. Heaster, and M. C. Skala, "Metabolic Imaging of Head and Neck Cancer Organoids," *PLoS One* **12**, e0170415 (2017).
16. K. P. Quinn, G. V. Sridharan, R. S. Hayden, D. L. Kaplan, K. Lee, and I. Georgakoudi, "Quantitative metabolic imaging using endogenous fluorescence to detect stem cell differentiation," *Sci. Rep.* **3**(1), 3432 (2013).
17. A. J. Walsh, K. M. Poole, C. L. Duvall, and M. C. Skala, "Ex vivo optical metabolic measurements from cultured tissue reflect in vivo tissue status," *J. Biomed. Opt.* **17**(11), 116015 (2012).
18. M. Skala and N. Ramanujam, "Multiphoton redox ratio imaging for metabolic monitoring in vivo," *Methods Mol. Biol.* **594**, 155–162 (2010).
19. B. Chance, B. Schoener, R. Oshino, F. Itshak, and Y. Nakase, "Oxidation-reduction ratio studies of mitochondria in freeze-trapped samples. NADH and flavoprotein fluorescence signals," *J. Biol. Chem.* **254**, 4764–4771 (1979).
20. B. Chance and G. Hollunger, "Energy-linked reduction of mitochondrial pyridine nucleotide," *Nature* **185**(4714), 666–672 (1960).
21. S. Jia, R. Wang, K. Wu, H. Jiang, and Z. Du, "Elucidation of the Mechanism of Action for Metal Based Anticancer Drugs by Mass Spectrometry-Based Quantitative Proteomics," *Molecules* **24**(3), 581 (2019).
22. M. Schenone, V. Danık, B. K. Wagner, and P. A. Clemons, "Target identification and mechanism of action in chemical biology and drug discovery," *Nat. Chem. Biol.* **9**(4), 232–240 (2013).
23. L. Zhang, E. Hatzakis, and A. D. Patterson, "NMR-Based Metabolomics and Its Application in Drug Metabolism and Cancer Research," *Curr. Pharmacol. Rep.* **2**(5), 231–240 (2016).
24. A. J. Walsh and M. C. Skala, "Optical metabolic imaging quantifies heterogeneous cell populations," *Biomed. Opt. Express* **6**(2), 559–573 (2015).
25. T. M. Heaster, B. A. Landman, and M. C. Skala, "Quantitative spatial analysis of metabolic heterogeneity across in vivo and in vitro tumor models," *Front. Oncol.* **9**, 1144 (2019).
26. I. Georgakoudi and K. P. Quinn, "Optical Imaging Using Endogenous Contrast to Assess Metabolic State," *Annu. Rev. Biomed. Eng.* **14**(1), 351–367 (2012).
27. R. M. Power and J. Huysken, "A guide to light-sheet fluorescence microscopy for multiscale imaging," *Nat. Methods* **14**(4), 360–373 (2017).
28. M. Weber and J. Huysken, "Light sheet microscopy for real-time developmental biology," *Curr. Opin. Genet. Dev.* **21**(5), 566–572 (2011).
29. P. Weber, S. Schickinger, M. Wagner, B. Angres, T. Bruns, and H. Schneckenburger, "Monitoring of apoptosis in 3D cell cultures by FRET and light sheet fluorescence microscopy," *Int. J. Mol. Sci.* **16**(12), 5375–5385 (2015).
30. I. Smyrek and E. H. K. Stelzer, "Quantitative three-dimensional evaluation of immunofluorescence staining for large whole mount spheroids with light sheet microscopy," *Biomed. Opt. Express* **8**(2), 484–499 (2017).
31. F. Pampaloni, B.-J. Chang, and E. H. K. Stelzer, "Light sheet-based fluorescence microscopy (LSFM) for the quantitative imaging of cells and tissues," *Cell Tissue Res.* **360**(1), 129–141 (2015).

32. T. M. Foley, S. N. Payne, C. A. Pasch, A. E. Yueh, D. R. Van De Hey, D. P. Korkos, L. Clipson, M. E. Maher, K. A. Matkowskyj, M. A. Newton, and D. A. Deming, "Dual PI3 K/mTOR Inhibition in Colorectal Cancers with APC and PIK3CA Mutations," *Mol. Cancer Res.* **15**(3), 317–327 (2017).
33. A. Kaufmann, M. Mickoleit, M. Weber, and J. Huiskens, "Multilayer mounting enables long-term imaging of zebrafish development in a light sheet microscope," *Development* **139**(17), 3242–3247 (2012).
34. J. Huiskens and D. Y. R. Stainier, "Selective plane illumination microscopy techniques in developmental biology," *Development* **136**(12), 1963–1975 (2009).
35. B. Mohelnikova-Duchonova, B. Melichar, and P. Soucek, "FOLFOX/FOLFIRI pharmacogenetics: The call for a personalized approach in colorectal cancer therapy," *World J. Gastroenterol.* **20**(30), 10316–10330 (2014).
36. R. Edmondson, J. J. Broglie, A. F. Adcock, and L. Yang, "Three-Dimensional Cell Culture Systems and Their Applications in Drug Discovery and Cell-Based Biosensors," *Assay Drug Dev. Technol.* **12**(4), 207–218 (2014).
37. C. A. Pasch, P. F. Favreau, A. E. Yueh, C. P. Babiarz, A. A. Gillette, J. T. Sharick, M. R. Karim, K. P. Nickel, A. K. DeZeeuw, C. M. Sprackling, P. B. Emmerich, R. A. DeStefanis, R. T. Pitera, S. N. Payne, D. P. Korkos, L. Clipson, C. M. Walsh, D. Miller, E. H. Carchman, M. E. Burkard, K. K. Lemmon, K. A. Matkowskyj, M. A. Newton, I. M. Ong, M. F. Bassetti, R. J. Kimple, M. C. Skala, and D. A. Deming, "Patient-Derived Cancer Organoid Cultures to Predict Sensitivity to Chemotherapy and Radiation," *Clin. Cancer Res.* **25**(17), 5376–5387 (2019).
38. A. T. Shah, M. Demory Beckler, A. J. Walsh, W. P. Jones, P. R. Pohlmann, and M. C. Skala, "Optical metabolic imaging of treatment response in human head and neck squamous cell carcinoma," *PLoS One* **9**(3), e90746 (2014).
39. K. J. Bode, S. Mueller, M. Schweinlin, M. Metzger, and T. Brunner, "A fast and simple fluorometric method to detect cell death in 3D intestinal organoids," *BioTechniques* **67**(1), 23–28 (2019).
40. L. Grassi, R. Alfonsi, F. Francescangeli, M. Signore, M. L. D. Angelis, A. Addario, M. Costantini, E. Flex, A. Ciolfi, S. Pizzi, A. Bruselles, M. Pallocca, G. Simone, M. Haoui, M. Falchi, M. Milella, S. Sentinelli, P. D. Matteo, E. Stellacci, M. Gallucci, G. Muto, M. Tartaglia, R. D. Maria, and D. Bonci, "Organoids as a new model for improving regenerative medicine and cancer personalized therapy in renal diseases," *Cell Death Dis.* **10**(3), 201 (2019).
41. E. Fujii, M. Yamazaki, S. Kawai, Y. Ohtani, T. Watanabe, A. Kato, and M. Suzuki, "A simple method for histopathological evaluation of organoids," *J. Toxicol Pathol.* **31**(1), 81–85 (2018).
42. K. Boehnke, P. W. Iversen, D. Schumacher, M. J. Lallena, R. Haro, J. Amat, J. Haybaeck, S. Liebs, M. Lange, R. Schäfer, C. R. A. Regenbrecht, C. Reinhard, and J. A. Velasco, "Assay Establishment and Validation of a High-Throughput Screening Platform for Three-Dimensional Patient-Derived Colon Cancer Organoid Cultures," *J. Biomol. Screening* **21**(9), 931–941 (2016).
43. C. Dunsby, "Optically sectioned imaging by oblique plane microscopy," *Opt. Express* **16**(25), 20306–20316 (2008).